

## Temperature-dependent material properties of Z-shaped MEMS thermal actuators made of single crystalline silicon

This content has been downloaded from IOPscience. Please scroll down to see the full text.

2013 J. Micromech. Microeng. 23 125036

(<http://iopscience.iop.org/0960-1317/23/12/125036>)

View [the table of contents for this issue](#), or go to the [journal homepage](#) for more

Download details:

IP Address: 152.14.115.185

This content was downloaded on 03/12/2013 at 18:24

Please note that [terms and conditions apply](#).

# Temperature-dependent material properties of Z-shaped MEMS thermal actuators made of single crystalline silicon

Jing Ouyang, Margaret McDonald and Yong Zhu

Department of Mechanical and Aerospace Engineering, North Carolina State University, Raleigh, NC 27695, USA

E-mail: [yong\\_zhu@ncsu.edu](mailto:yong_zhu@ncsu.edu)

Received 27 August 2013

Published 15 November 2013

Online at [stacks.iop.org/JMM/23/125036](http://stacks.iop.org/JMM/23/125036)

## Abstract

MEMS thermal actuators have been employed in a broad range of applications, often operating in different environments (e.g. vacuum, air or liquid). Since the involved heat dissipation mechanisms are different in different operating environments, the device performances are expected to be different. In this paper, we report experimental measurement and multiphysics modeling of device performance metrics of a recently introduced thermal actuator, the Z-shaped thermal actuator, including temperature distribution, electric resistance and displacement in both air and vacuum environments. The temperature measurement was based on Raman scattering in air. Fully 3D multiphysics (coupled thermo-electro-mechanical) simulations were performed to treat both air and vacuum environments. Heat conduction through air to neighboring devices is important, while heat convection to air is negligible. The experimental and modeling results agreed well, which demonstrated the accuracy of the temperature-dependent material properties used in the modeling. Fully 3D multiphysics modeling combined with valid material property parameters will enable the exploration of the design space and the optimization of performances of the MEMS thermal actuators for different operating environments.

(Some figures may appear in colour only in the online journal)

## 1. Introduction

In the field of microelectromechanical systems (MEMS), thermal actuators operate at low actuation voltage but provide compact, stable and high-force loading. MEMS thermal actuators with different topographies have been demonstrated for in-plane actuation, including U-shape [1, 2], V-shape [3, 4] and Z-shape [5], with complementary features. These actuators are employed in a broad range of applications including an on-chip nanoscale material testing system [6–8], a nanopositioner [9, 10] and a micro-gripper for single cell manipulation [11, 12], often operating in different environments (e.g. vacuum, air or liquid). As an example, thermal actuators have been used for nanomechanical testing inside scanning/transmission electron microscopes (in vacuum) [7] or under an optical microscope (in air) [13]. The involved heat dissipation mechanisms are different in different operating

environments; it is thus of relevance to measure how such a difference impacts the resulting temperature distribution, electric resistance and actuator displacement. In the case of Z-shaped thermal actuators (ZTAs) [5, 14], their displacement and electric resistance have been characterized in vacuum, but not in air. In addition, no temperature measurement has been reported.

On the other hand, it is useful to explore the design space and optimize the performances of the MEMS thermal actuators for different operating environments. For this purpose, multiphysics modeling including electric, thermal and structural (mechanical) domains plays an important role [15–18]. One requirement as well as a challenge for multiphysics modeling is accurate material properties, more specifically the temperature-dependent ones [19]. A comparison of device performance metrics between modeling and experiments could provide an indirect method

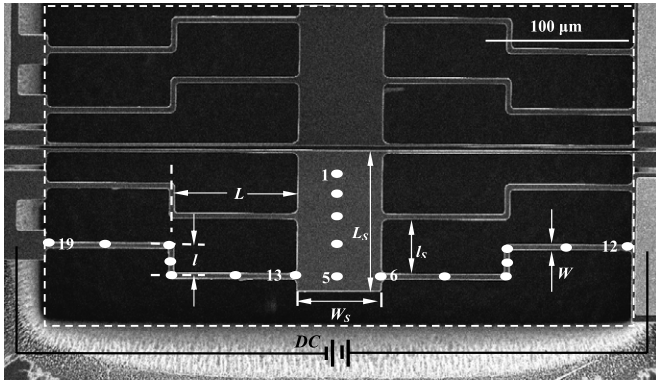


**Figure 1.** SEM image of a ZTA with a neighboring (reference) device on top. 19 different positions are marked for temperature measurement. The dashed box defines the area for multiphysics simulations in air (figure 6). The current flows through the Z-shaped beams. The eccentricity is marked as  $l$  in the figure. Note that the straight beams are heat sink beams as reported in [16, 20].

to determine or at least validate these property parameters, especially under multiple operation environments (e.g. vacuum and air).

In this paper, we report the experimental measurement and multiphysics modeling of the device performance metrics of a ZTA including displacement, electric resistance and temperature distribution in both air and vacuum. The temperature measurement was based on Raman scattering in air. Fully 3D multiphysics (coupled thermo-electro-mechanical) simulations were performed to treat both air and vacuum environments. The experimental and modeling results agreed well, which demonstrated the accuracy of the temperature-dependent material properties used in the modeling. This paper begins with a brief description of the ZTA followed by the experimental methods to measure the device performances as well as the multiphysics modeling. Then the modeling and experimental results of the device performances are discussed. Comparison between the experimental and modeling results plus additional parametric study are put forth to determine the material property parameters.

## 2. Experimental and modeling methods

### 2.1. Z-shaped thermal actuator

The ZTA is a relatively new member in the family of thermal actuators and could be complementary to the widely used comb drives and V-shaped thermal actuators. It consists of a suspended shuttle supported by two symmetric arrays of thin beams that are anchored to the substrate, as shown in figure 1. The ZTA dimensions are listed in table 1. Note that the dots in figure 1 are positions where temperature measurement was taken (to be described later). These beams are Z-shaped, kinked toward the direction of the desired displacement. When a voltage is applied across the actuator, the Joule heating effect generates heat and temperature rise in the beams. As a result, the beams expand. Due to the short vertical beam in the Z-shape design (eccentricity as defined in figure 1) and the overall symmetry, the Z-shaped beam deflects and moves the central shuttle forward (downwards in

**Table 1.** Dimensions of the Z-shaped thermal actuator used in simulations.

Dimension	Symbol	Value	Unit
Beam length	$L$	88	$\mu\text{m}$
Beam width	$W$	4	$\mu\text{m}$
Thickness	$t$	10	$\mu\text{m}$
Eccentricity	$l$	20	$\mu\text{m}$
Shuttle length	$L_S$	92	$\mu\text{m}$
Shuttle width	$W_S$	60	$\mu\text{m}$
Beam spacing	$l_S$	42	$\mu\text{m}$

figure 1). The geometry of the ZTA amplifies the relatively small thermal expansion in beams to achieve a much larger displacement of the center shuttle. The ZTAs were fabricated at MEMSCAP (Durham, NC) using the silicon-on-insulator multi-user MEMS processes. The structure layer is  $n$ -type (phosphorus-doped) single crystalline silicon (SCS).

### 2.2. Experimental method

The device performances such as displacement and electric resistance were measured in both vacuum and air, while the temperature distribution was only measured in air due to the employment of Raman spectroscopy [20, 21]. The measurements in vacuum were conducted inside a scanning electron microscope (SEM) via an electric feedthrough [5]; the displacement resolution is about 1 nm. To measure the electric resistance, the voltage across the ZTA was measured at a given current. The measurements of displacement and temperature distribution in air are described in detail below.

The ZTA displacement in air was measured under an optical microscope ( $100\times$ ) using edge detection, an image correlation method. A series of optical images of the ZTA were taken at different current levels (figure 2(a)). ImageJ was used to process the images. It was used first to enhance the contrast of the edges (figure 2(b)), then to plot the grayscale (i.e. intensity value) along a line across two edges, defined in figure 2(b); one edge is of the ZTA and the other is of a stationary reference device. The distance between these two devices is  $2\mu\text{m}$  when no current is applied. Two intensity distributions at two different current levels are shown in figures 2(c) and (d) for comparison. Following an algorithm developed previously for edge detection [6], the ZTA displacement was obtained in terms of number of pixels. Using the calibration factor of the optical image at the given magnification, the displacement was converted from pixel to nanometer. The displacement for 8 mA current in air is  $0.29\mu\text{m}$ , measured by comparing figures 2(c) and (d). Since ImageJ offers subpixel resolution (e.g., one-tenth of a pixel), 7 nm displacement resolution was obtained in our measurement.

The temperature distribution of the ZTA in air was measured using a HORIBA LabRAM HR Raman microscope. The excitation source was a 633 nm laser. The laser power on the sample was kept below  $3\mu\text{W}$  to avoid laser-induced local heating, using the D4 filter. The objective lens was  $100\times$  with a numerical aperture of 0.9. The focused laser spot was about  $1\mu\text{m}$  in diameter. The Raman signal was collected in backscatter through the microscope objective, relayed to

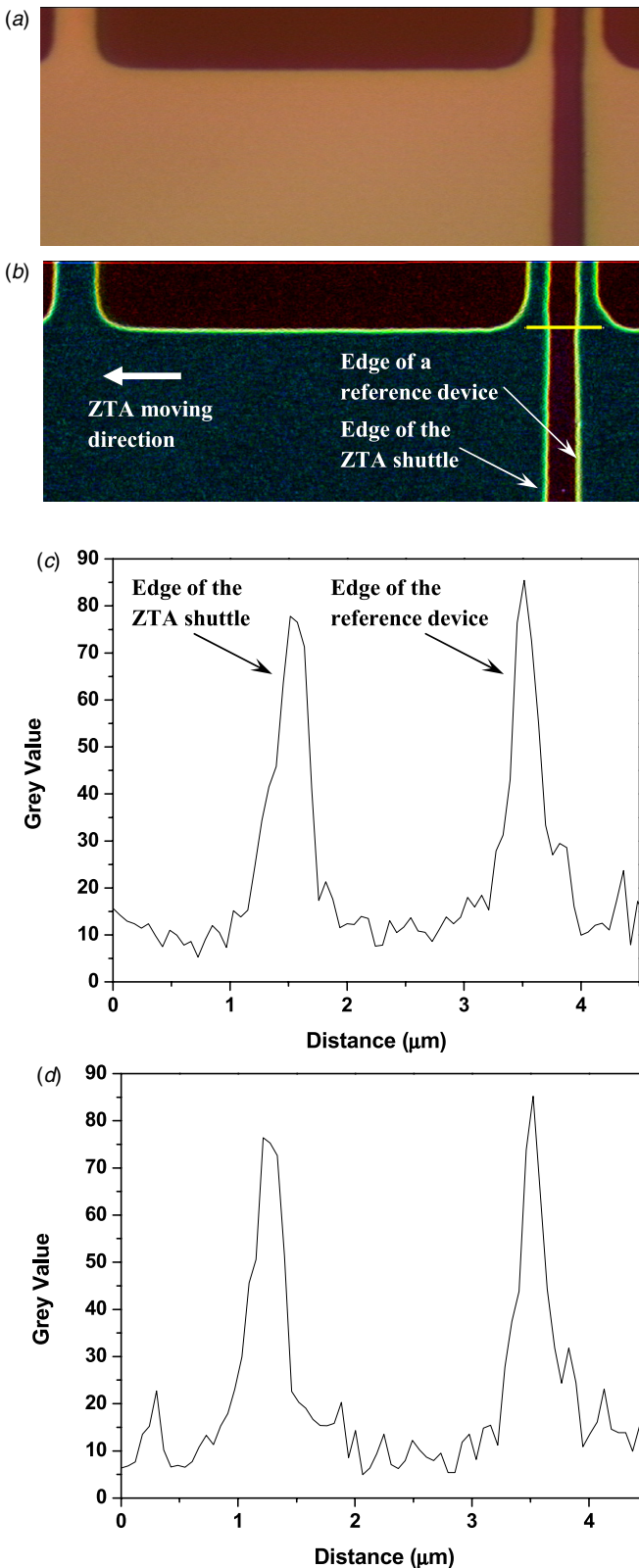


**Figure 2.** Displacement measurement using optical microscopy in air. (a) Optical image of the ZTA. (b) The image in (a) after the contrast enhancement. (c) The grayscale value along a defined line across the gap (as shown in panel (b)) at zero applied current. The two peaks represent the edge of the ZTA shuttle and the edge of the neighboring device. (d) The grayscale value at 8 mA applied current.

a grating spectrograph and detected using a deep-depletion, thermoelectrically cooled CCD camera. Each measurement took approximately 60 s.

Raman scattering is an inelastic light scattering process in which a small fraction of incident photons from a light source couple with the optical phonon modes of the solid-state medium and are scattered at frequencies that are shifted by the phonon vibrational energies. The Raman interaction leads to two possible outcomes: Stokes Raman scattering (the material absorbs energy and the emitted photon has a lower energy than the absorbed photon) and anti-Stokes Raman scattering (the material loses energy and the emitted photon has a higher energy than the absorbed photon). With increasing temperature, the location of the Raman peak shifts toward lower phonon energy, the Raman spectrum is broadened and the intensity of the anti-Stokes signature relative to the Stokes-shifted line increases. Kearney *et al* found the peak position of the Stokes-shifted Raman spectrum to be a robust indicator of temperature compared to the other two measures [21]; therefore, the Stokes shift was recorded in our experiments.

### 2.3. Modeling method

Nonlinear multiphysics finite element simulation was carried out using ANSYS 13.0 to study the displacement, electric resistance and temperature distribution of the ZTA. The ZTA behaviors were simulated both in vacuum and in air. For the vacuum environment, the only heat dissipation mechanism is the heat conduction through the device itself to the anchors (substrate). For the air environment, two additional heat dissipation mechanisms could contribute: the thermal conduction through the air to the silicon substrate and neighboring devices, and the thermal convection from the ZTA to the air. The thermal radiation was not considered in our simulations.

The simulation is a coupled-field analysis involving electric, thermal and mechanical fields. The input is the electric current across the ZTA and the output includes the actuator temperature and displacement fields. Temperature increase in the anchors (i.e. contact pads) is neglected due to the relatively low temperature increase in this work; therefore, thermal boundary conditions are zero temperature change at the anchors for the vacuum environment, but zero temperature change at the anchors, the surrounding substrate and the neighboring device (e.g. the reference device on top of the anchors of the ZTA in figure 1) for the air environment. The mechanical boundary conditions are fixed displacements at the anchor sites. Element type SOLID 98 was used for the ZTA, the neighboring device and the surrounding substrate and SOLID 70 (heat transfer element) was used for the air. The laboratory temperature during the Raman experiments (296 K) is set as the reference temperature in the simulations. The material parameters used in the simulations are listed in table 2.

### 3. Results and discussion

The Raman spectra are typically fit to a Voigt lineshape function to determine the Stokes peak location. Figure 3 shows

**Table 2.** Material parameters used in simulations. Note that the unit for temperature in this paper is Kelvin.

Parameter	Symbol	Value	Unit
Young's modulus, silicon [5]	$E$	160	GPa
Poisson's ratio, silicon [5]	$\nu$	0.28	–
Density, silicon	$\rho$	2330	kg m <sup>-3</sup>
Specific heat, silicon	$C$	710	J (kgK) <sup>-1</sup>
Thermal conductivity, silicon (temperature-dependent) [23]	$K_S(T)$	$210\,658 \times T^{-1.2747}$	W (mK) <sup>-1</sup>
Thermal expansion coefficient, silicon (temperature-dependent) [19]	$\alpha(T)$	$-4 \times 10^{-12} T^2 + 8 \times 10^{-9} T + 4 \times 10^{-7}$	K <sup>-1</sup>
Electric resistivity, silicon (temperature-dependent) [5]	$\rho(T)$	$7.15 \times 10^{-5} [1 + 3 \times 10^{-3} (T-273)]$	$\Omega\text{m}$
Thermal conductivity, air [20]	$K_{\text{air}}$	0.026	W (mK) <sup>-1</sup>
Convection heat transfer coefficient, air [24]	$C_{\text{air}}$	100	W (m <sup>2</sup> K) <sup>-1</sup>

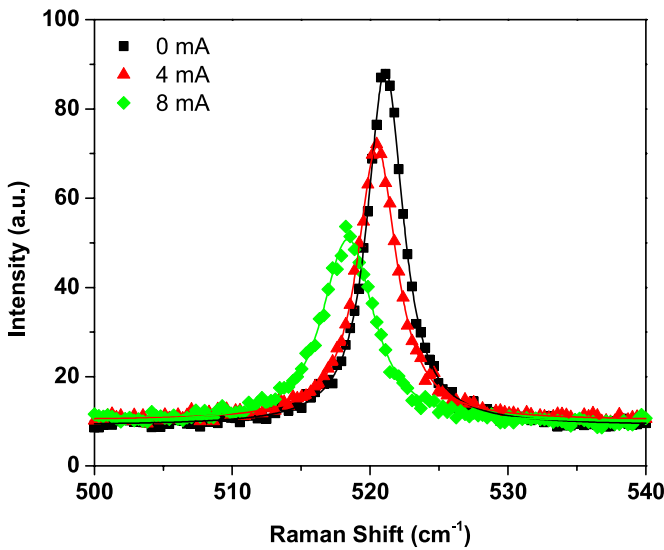


**Figure 3.** Three representative Stokes-shifted Raman spectra (with the Voigt fitting) at different current levels.

representative Stokes-shifted Raman spectra at three different current levels. To calibrate the Raman (Stokes) shift as a function of temperature, a MEMS chip containing many ZTAs was placed on top of a hot plate. A large area of the device layer was chosen, where both the Raman scattering and the infrared thermometer-based temperature measurement were conducted. The Raman spectrum was fit to the Voigt function to determine the Stokes peak location. Figure 4 shows the Raman shift as a function of the substrate temperature, which follows a linear relationship given by

$$\Delta T = \frac{\Omega - \Omega_0}{-0.0242 \text{ cm}^{-1}} K \quad (1)$$

where  $\Omega_0$  and  $\Omega$  are the measured peak positions at the laboratory temperature of 296 K and at the operating temperature, respectively. Note that the substrate used for the Raman calibration is made of the same *n*-type SCS as the ZTAs are. Following equation (1), the ‘measured’ temperatures for different applied temperatures were calculated and plotted as the second y-axis in figure 4. Comparing the measured and applied temperatures, we obtained the uncertainty of temperature measurement using our Raman microscope as  $\pm 0.34$  K.

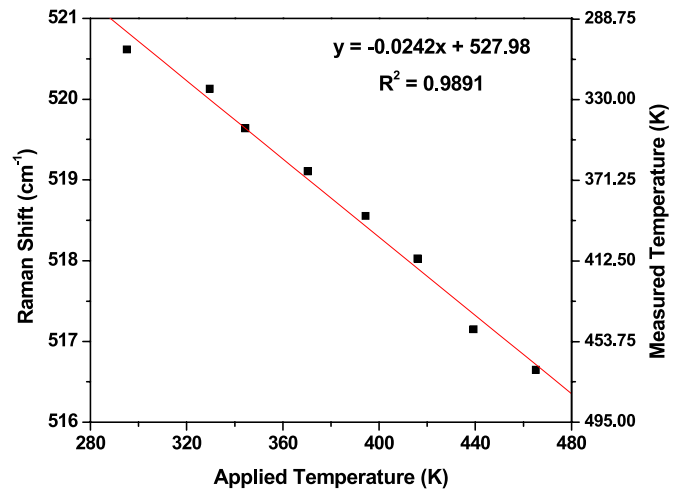


**Figure 4.** Calibration curve of the peak position of Raman spectra versus temperature for a (1 0 0) oriented SCS surface.

The multiphysics simulations of the ZTA were carried out for both vacuum and air environments. The ZTA dimensions used in the ANSYS model are identical to those of the real device, as listed in table 1. Temperature-dependent parameters were used; for instance, the electric resistivity of the doped SCS used to fabricate our ZTAs could vary due to the doping concentration, temperature, etc. The temperature coefficient of resistance (TCR) of doped SCS used in our simulation is  $3 \times 10^{-3} \text{ K}^{-1}$ . TCR ranges from negative to positive for semiconductors depending on the doping level [22]. In this work, the positive TCR within the typical range for heavily doped SCS is discussed. Figure 5 shows the displacement and temperature contours in vacuum, while figure 6 shows them in air. As mentioned above, in vacuum, the only heat dissipation mechanism is through the Z-shaped beams to the substrate. As shown in figure 5(a), the highest temperature increase at 8 mA current is 143.6 K, which is located on the Z-shaped beam close to the shuttle. Note that the highest temperature is not at the middle of the shuttle due to the presence of two heat sink beams (on top). A heat sink beam that can be co-fabricated with the device provides an effective way to control the temperature distribution, especially in vacuum where no other heat dissipation mechanisms are available [20]. In air, two additional heat dissipation mechanisms are

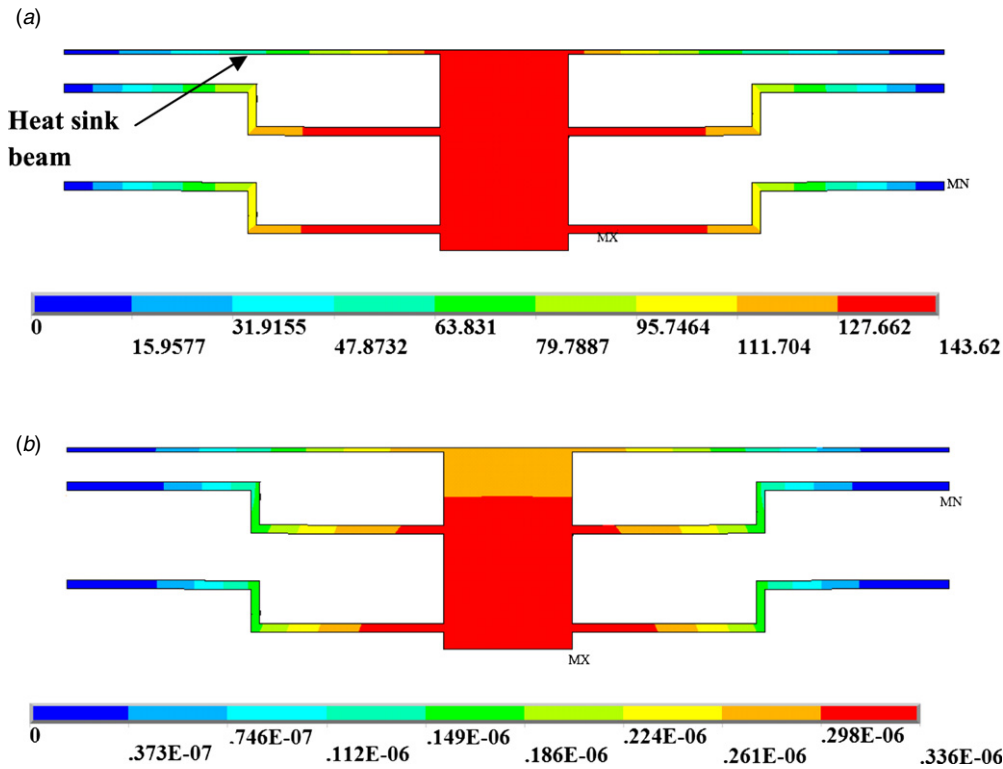


**Figure 5.** (a) Temperature change and (b) displacement contours of the ZTA in vacuum at 8 mA current. The highest displacement/temperature is marked as MX, the lowest one is marked as MN. The unit is K for the temperature change and meter for the displacement.

**Table 3.** Temperature measurement results at all 19 positions under different current levels. The unit of the temperature is K.

	0 mA	1 mA	2 mA	3 mA	4 mA	5 mA	6 mA	7 mA	8 mA
Position 1	295.6	297.7	301.8	310.1	320.4	331.5	349.3	372.9	409.2
Position 2	295.6	301.0	302.6	310.1	319.6	332.0	353.4	377.0	413.8
Position 3	295.6	296.0	301.4	303.9	315.8	329.1	346.8	372.9	413.8
Position 4	295.6	295.6	300.1	308.8	320.0	328.7	349.3	378.2	409.2
Position 5	295.6	298.5	305.1	313.4	320.0	331.1	353.9	382.0	420.0
Position 6	295.6	298.9	302.2	311.3	313.4	330.7	350.1	379.1	418.3
Position 7	295.6	297.3	301.8	303.0	313.4	327.0	348.1	376.6	415.0
Position 8	295.6	298.1	301.8	310.1	314.2	325.4	341.5	368.3	401.4
Position 9	295.6	296.4	299.3	305.1	315.8	322.9	338.6	361.7	392.7
Position 10	295.6	297.3	301.0	307.2	318.3	328.2	342.7	364.6	393.1
Position 11	295.6	296.0	298.1	301.0	305.9	311.7	321.2	332.8	348.5
Position 12	295.6	298.1	297.7	300.1	299.7	303.9	306.3	308.4	307.6
Position 13	295.6	296.8	297.7	305.9	316.7	330.3	349.3	378.2	419.6
Position 14	295.6	299.7	300.1	306.8	317.5	329.9	352.6	379.9	419.1
Position 15	295.6	299.7	301.0	309.2	319.2	329.1	347.2	374.5	409.2
Position 16	295.6	298.9	303.5	303.9	315.4	324.1	344.4	368.7	401.0
Position 17	295.6	296.4	300.6	306.3	320.8	329.9	348.1	369.6	398.1
Position 18	295.6	296.0	299.7	301.0	307.2	313.8	324.9	339.8	363.4
Position 19	295.6	297.3	296.4	301.8	302.6	296.8	297.7	300.6	304.3

heat conduction to the neighboring device through an air gap and heat convection to air. Our simulations considered both additional dissipation mechanisms. For instance, at 8 mA current, the maximum temperature increase is 139.3 K and 122 K considering heat convection only and heat conduction to the neighboring device only, respectively. If considering both dissipation mechanisms, the maximum temperature increase is 119.4 K as shown in figure 6(a). Therefore, the heat conduction to the neighboring device through an air gap is considerable

(21.6 K difference from the vacuum environment), while the heat convection to the air is modest (4.3 K difference). At 8 mA current, displacements of 0.336  $\mu\text{m}$  and 0.254  $\mu\text{m}$  and electric resistances of 479.6  $\Omega$  and 461.6  $\Omega$  are obtained for vacuum and air environments, respectively.

Clearly, heat conduction to the neighboring device plays an important role in the temperature and other device performances (e.g., displacement and electric resistance) of the ZTA. To further evaluate the effect of heat dissipation to

**Table 4.** All 12 positions temperature simulated results at different current levels. The unit of temperature is K.

	0 mA	1 mA	2 mA	3 mA	4 mA	5 mA	6 mA	7 mA	8 mA
Position 1	295.6	296.7	300.1	305.9	314.6	326.7	343.2	365.8	399.5
Position 2	295.6	296.7	300.1	306.0	314.7	326.9	343.5	366.2	400.2
Position 3	295.6	296.7	300.1	306.1	314.8	327.1	343.9	366.9	401.3
Position 4	295.6	296.7	300.2	306.2	314.9	327.3	344.3	367.4	402.1
Position 5	295.6	296.7	300.2	306.2	315.1	327.5	344.6	368.0	403.0
Position 6	295.6	296.7	300.2	306.3	315.2	327.7	344.9	368.4	403.7
Position 7	295.6	296.7	300.3	306.3	315.4	328.0	345.5	369.4	405.2
Position 8	295.6	296.6	299.6	304.9	312.6	323.4	338.0	357.8	386.6
Position 9	295.6	296.5	299.4	304.3	311.5	321.6	335.2	353.4	379.7
Position 10	295.6	296.5	299.2	303.9	310.7	320.3	333.1	350.3	374.9
Position 11	295.6	296.1	297.7	300.8	304.7	309.7	317.3	326.7	338.4
Position 12	295.6	295.6	295.6	295.6	295.6	295.6	295.6	295.6	295.6

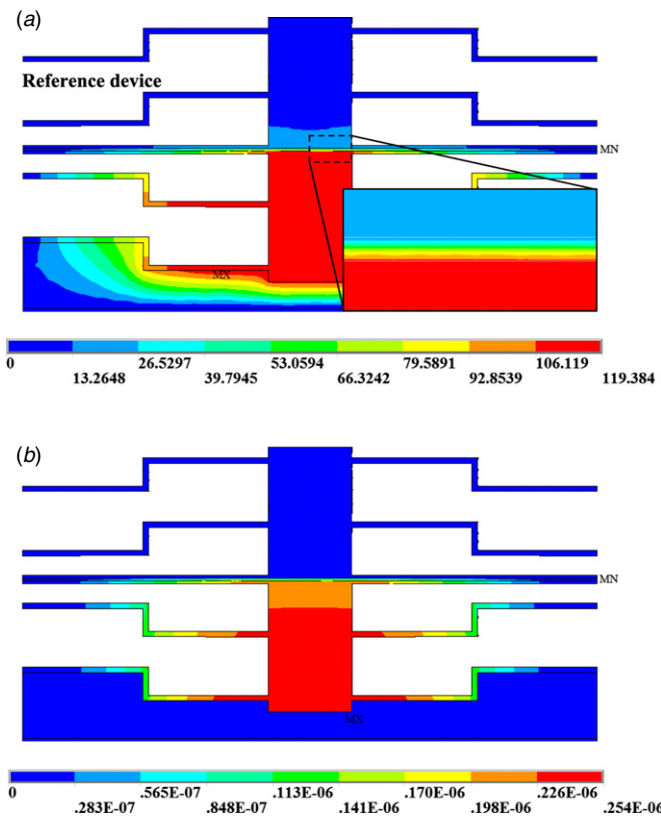


**Figure 6.** (a) Temperature change and (b) displacement contours of the ZTA in air at 8 mA current. The bottom device is of interest. The highest displacement/temperature is marked as MX, the lowest one is marked as MN. The unit is K for the temperature change and meter for the displacement. The inset in (a) shows a magnified view of the temperature distribution across the gap.

the neighboring device, we systematically varied the distance of the air gap. Figure 7 shows the temperature at position 1 as a function of the air gap distance. When the air gap is small (e.g. 1  $\mu\text{m}$ ), the heat loss through the gap is important, causing nearly 40 K decrease in temperature (for 8 mA current). When the air gap is large (e.g. >20  $\mu\text{m}$ ), the heat loss through the gap is negligible. This provides a valuable design guideline for MEMS thermal actuators.

The temperature measurements were performed on a total of 19 positions on the ZTA as marked by dots in figure 1. Table 3 lists all the measured temperatures at these positions

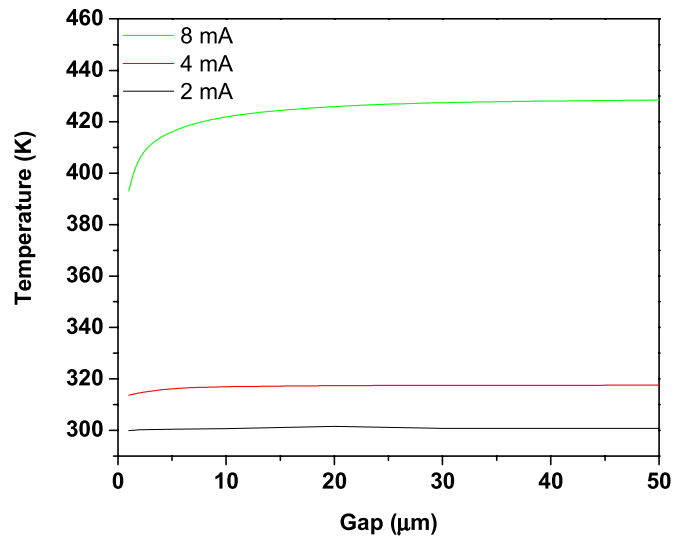


**Figure 7.** The temperature at position 1 as a function of the gap size and the applied current.

under different applied current levels. Positions 1–5 are on the shuttle, positions 6–12 are on the right beam and positions 13–19 are on the left beam. Indeed, positions 6–12 and 13–19 are symmetric. The purpose of measuring the temperatures along the symmetric beams was to obtain redundant data and provide another way to check the measurement accuracy. Positions 12 and 19 are anchoring points of the ZTA. Figure 8(a) shows the measured temperature as a function of the applied current for three representative positions (positions 1, 7 and 11), while figure 8(b) shows the temperature at 12 positions (1–12) under three different current levels. From table 3, it can be seen that the temperature distribution along the two beams follow the symmetry very well.

The simulated results of temperature are listed in table 4. Since the left beam and the right beam are purely symmetric in the simulations, only the temperature values on the right beams are given. The simulated temperatures at the three positions and at three current levels are also plotted in figures 8(a) and (b), respectively. The simulated temperatures as shown in figure 8 are on the ZTA surface, which is consistent with the Raman measurement. Figures 8(a) and (b) show good agreement between the experimental and simulation results except at higher current levels where a discrepancy less than

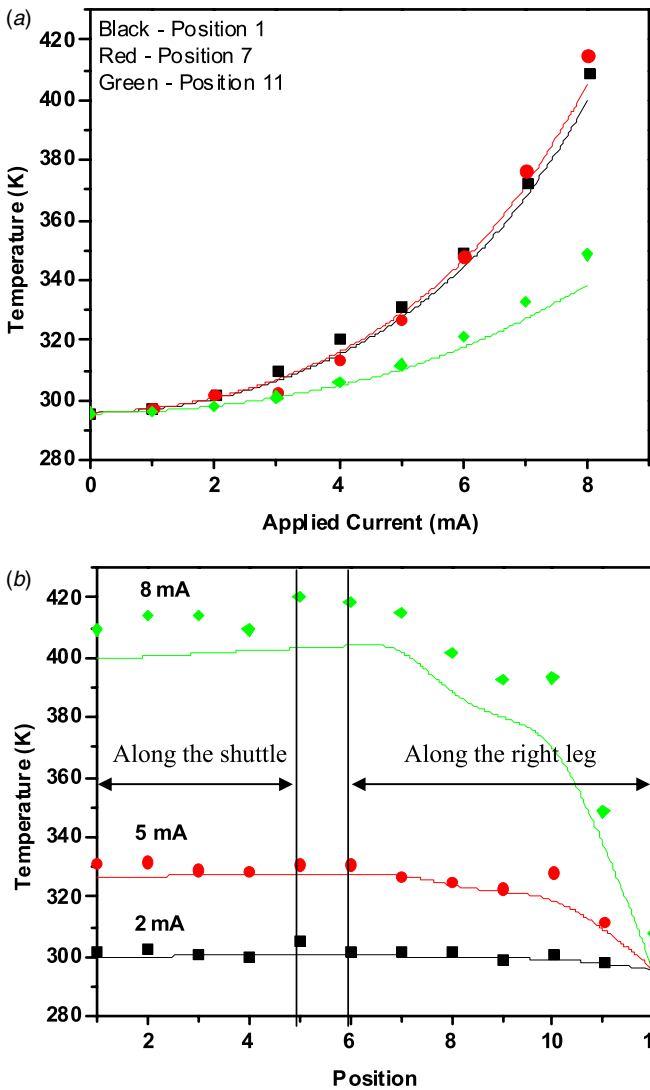


**Figure 8.** (a) Experimental and simulation results of temperature versus applied current at three different positions: 1, 7 and 11. The dots are experimental results and the lines are simulation results. (b) Experimental and simulation results of temperature versus position at three different current levels: 2, 5 and 8 mA. Positions 1–5 are along the shuttle length, while positions from 5 to 12 represent (symmetrically) half of the ZTA.

20 K can be seen. Such a discrepancy could come from several sources, such as laser-induced heating, instrument drift, accuracy of peak location, temperature-induced axial stress and the slope of the calibration curve fit. Since our laser power was kept below  $3 \mu\text{W}$ , the laser-induced heating was negligible. Instrument drift was identified to cause  $\pm 9 \text{ K}$  error over the course of one day [21]. However, our measurement at each position took only  $\sim 1 \text{ min}$ . In addition, before measuring each position on the device, we measured the substrate as reference. Temperature at each position was then deduced based on the relative change in peak location. Therefore, instrument drift was negligible too. The accuracy of peak location was assumed to cause less than  $\pm 3 \text{ K}$  error for the temperature range in this work (from room temperature up to 420 K) [21], since the same fitting method was used to fit the Raman data. Our FEM modeling found that the maximum

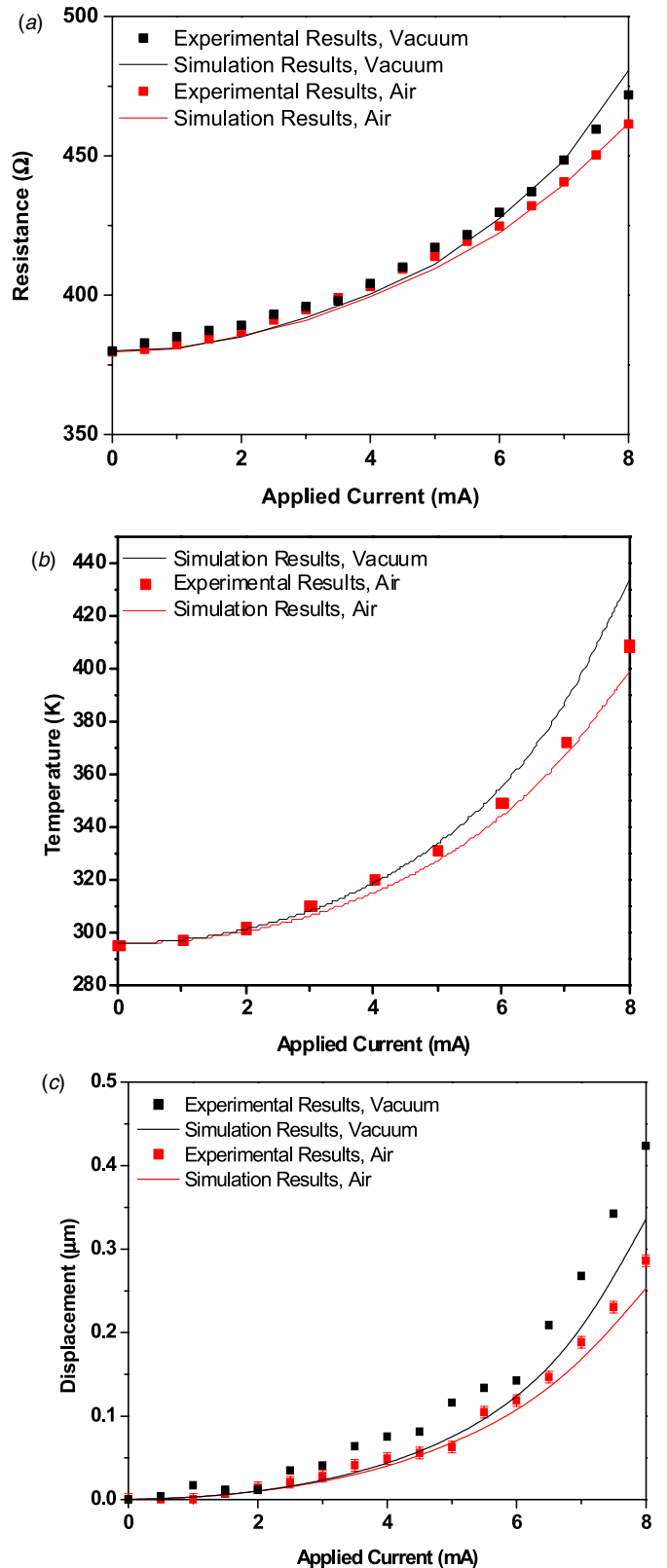


**Figure 9.** Comparison between experimental and simulation results of (a) electric resistance, (b) temperature at position 1 and (c) the maximum displacement (at the front edge of the shuttle). The results are under both air and vacuum environments when possible.

stress in our temperature range was no more than 40 MPa, so stress-induced error was estimated to be  $\pm 1.5 \text{ K}$  [21].

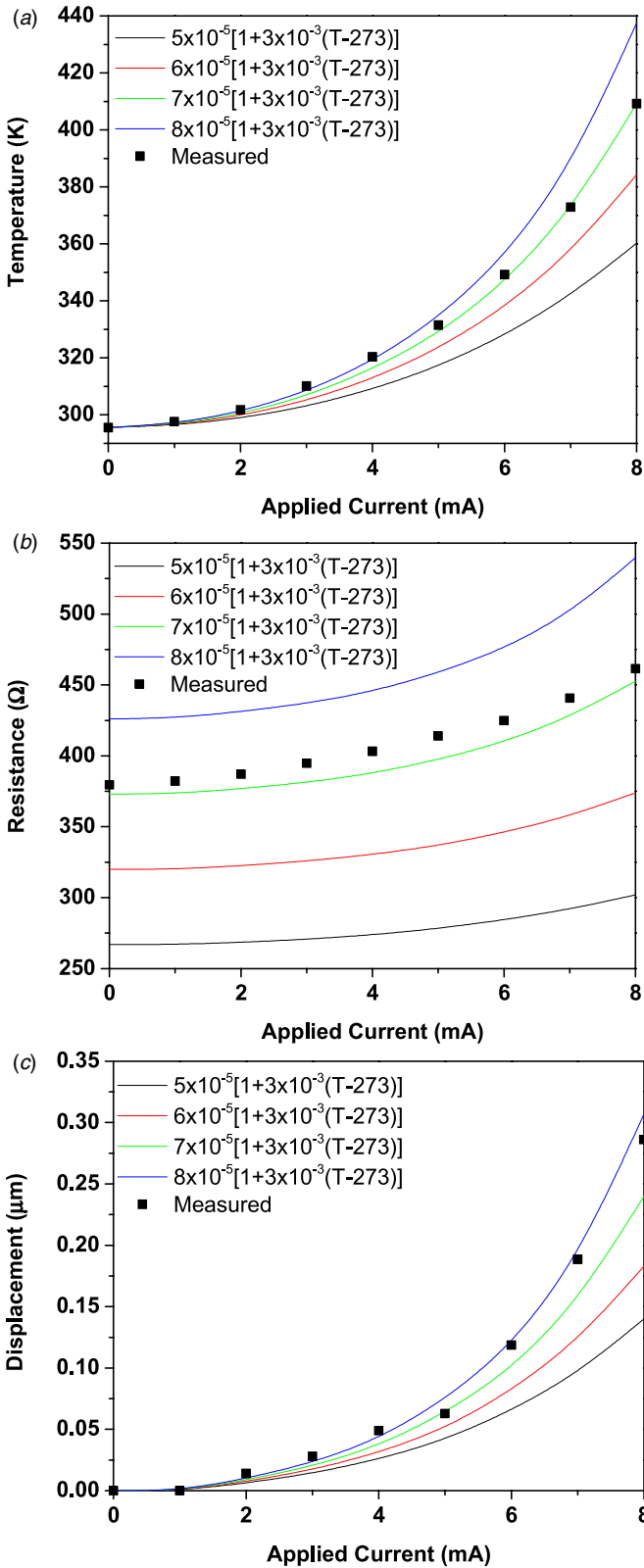


**Figure 10.** Simulation results of (a) temperature, (b) electric resistance and (c) displacement as a function of applied current at four different resistivity expressions at position 1.

Error in estimating the slope of the linear fit to the calibration data in figure 4 was found to be  $\pm 0.34$  K. Overall, the total uncertainty was estimated to  $\pm 3.4$  K using vector summation.

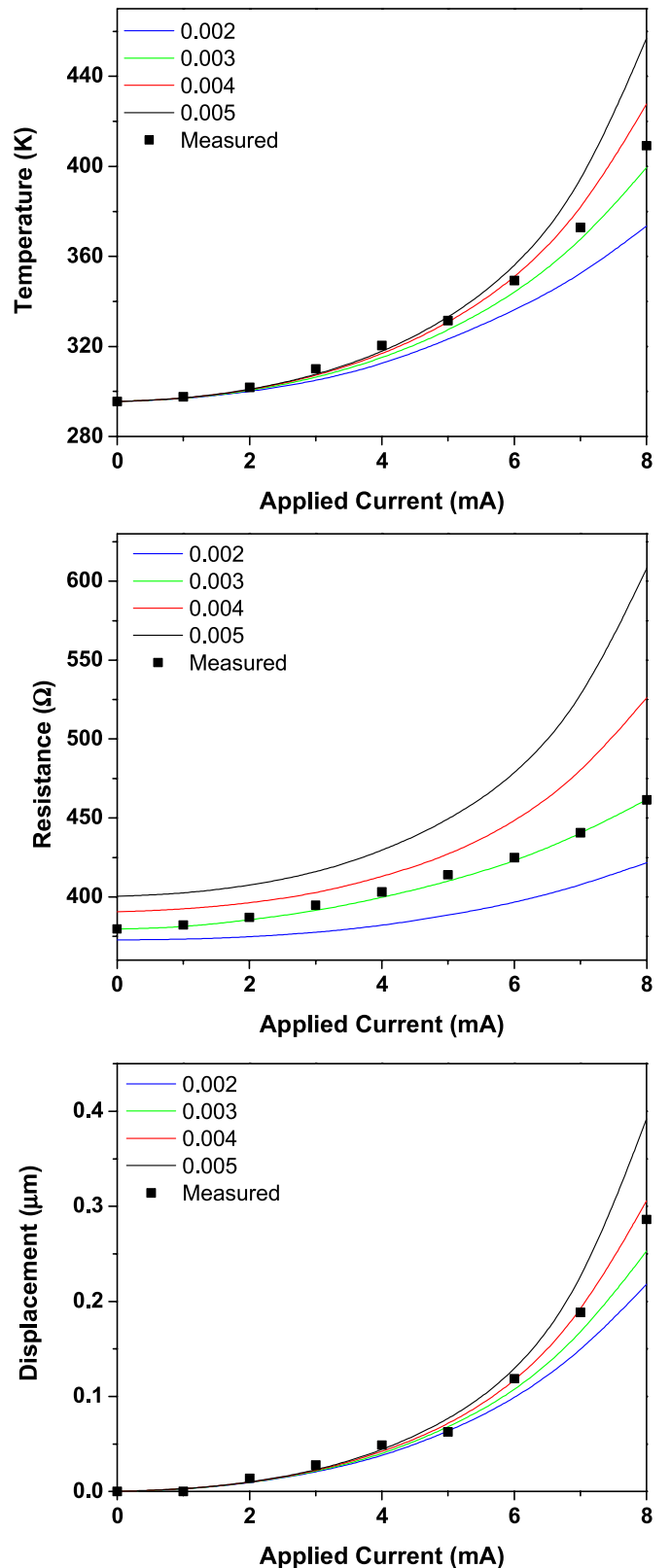


**Figure 11.** Simulation results of (a) temperature, (b) electric resistance and (c) displacement as a function of applied current at four different TCR values at position 1.

Such an uncertainty is slightly larger than that ( $\pm 1.5$  K) for SCS fabricated by SOI-MUMPS [17], and smaller than that ( $\pm 10$  K) for polysilicon [21]. Another possible source is the

temperature boundary condition used in the simulations. The anchors are assumed to remain at room temperature but in reality could be modestly heated [18]. In fact, our Raman thermometry results showed that the two points (12 and 19) near the anchors were heated up to 12 K at 8 mA current; see table 3 and figure 8(b).

The experimental and simulation results on the electric resistance, the temperature at position 1 and the maximum displacement (at the front edge of the shuttle) are compared, as shown in figure 9. Note that all three parameters are reported for both vacuum and air environments except the temperature, for which only the experimental results in air exist. The temperature at position 1 is of relevance for many applications since the specimen is connected to this end. Nearly all the comparisons agree very well, which is actually very challenging to achieve in view of the fact that many material property parameters are involved with some temperature-dependent parameters. This indicates the overall accuracy of the material properties used in this work.

To further validate the material property parameters, we could systematically vary them and evaluate the results. Since the parameters we used led to good agreement with experiments, we did not perform the extensive parametric study but rather focused on one parameter, electric resistivity, as an example. Four different resistivity expressions were employed. The simulated electric resistances, temperatures and displacements at position 1 in air with varying prefactors (i.e. room temperature resistivity) are shown in figure 10 as functions of the applied current level. The device performances with varying TCR are shown in figure 11. Figures 10 and 11 show that the device performances highly depend on the prefactor and TCR. In view of the close agreement between experiments and simulations as shown in figure 9, these parametric studies validated the resistivity expression used in this work.

#### 4. Conclusions

We report a comprehensive investigation of the device performances of ZTAs by combined experimental measurement and multiphysics modeling. The highest temperature in air was found to be 24.2 K lower than that in vacuum for 8 mA applied current. Heat conduction through air to neighboring devices is important, while heat convection to air is negligible. It was found that at least 20  $\mu\text{m}$  gap is required between the ZTA and the neighboring device so that the ZTA can be considered as thermally isolated. In terms of modeling thermal actuators, most of the literature reports are only for the vacuum environment, where heat dissipation to air is either neglected [2] or treated in specific cases (e.g. 1D model to account for heat conduction through air to substrate) [18]. The fully 3D multiphysics modeling reported here takes into account heat dissipation to air. In addition, the material property parameters used in this work are found to provide realistic results that agree well with the experimental results in terms of major device performances (e.g. temperature distribution, displacement and electric resistance). Fully 3D multiphysics

modeling combined with validated material property parameters, as demonstrated in this work, will find broad applications for MEMS devices fabricated by the SOI-MUMPs.

#### Acknowledgments

This work was supported by the National Science Foundation under award no. CMMI-1030637. The *in situ* SEM experiments were performed in the Analytical Instrumentation Facility at North Carolina State University.

#### References

- [1] Comtois J H and Bright V M 1996 Surface micromachined polysilicon thermal actuator arrays and applications *Tech. Dig. of Solid State Sensor and Actuator Workshop (Hilton Head Island, SC, June 3–6)* pp 174–7
- [2] Huang Q A and Lee N K S 1999 Analytical modeling and optimization for a laterally-driven polysilicon thermal actuator *Microsyst. Technol.* **5** 133–7
- [3] Cragun R and Howell L L 1999 Linear thermomechanical microactuators *ASME Int. Mechanical Engineering Congress and Exposition* pp 181–8
- [4] Que L, Park J S and Gianchandani Y B 2001 Bent-beam electrothermal actuators—part I: single beam and cascaded devices *J. Microelectromech. Syst.* **10** 247–54
- [5] Guan C H and Zhu Y 2010 An electrothermal microactuator with Z-shaped beams *J. Micromech. Microeng.* **20** 85014
- [6] Zhu Y, Moldovan N and Espinosa H D 2005 A microelectromechanical load sensor for *in situ* electron and x-ray microscopy tensile testing of nanostructures *Appl. Phys. Lett.* **86** 13506
- [7] Zhu Y and Espinosa H D 2005 An electromechanical material testing system for *in situ* electron microscopy and applications *Proc. Natl Acad. Sci. USA* **102** 14503–8
- [8] Espinosa H D, Zhu Y and Moldovan N 2007 Design and operation of a MEMS-based material testing system for nanomechanical characterization *J. Microelectromech. Syst.* **16** 1219–31
- [9] Park J S, Chu L L, Oliver A D and Gianchandani Y B 2001 Bent-beam electrothermal actuators—part II: linear and rotary microengines *J. Microelectromech. Syst.* **10** 255–62
- [10] Maloney J M, Schreiber D S and DeVoe D L 2004 Large-force electrothermal linear micromotors *J. Micromech. Microeng.* **14** 226–34
- [11] Chronis N and Lee L P 2005 Electrothermally activated SU-8 microgripper for single cell manipulation in solution *J. Microelectromech. Syst.* **14** 857–63
- [12] Luo J K, Flewitt A J, Spearing S M, Fleck N A and Milne W I 2005 Comparison of microtweezers based on three lateral thermal actuator configurations *J. Micromech. Microeng.* **15** 1294–302
- [13] Hazra S S, Baker M S, Beuth J L and de Boer M P 2009 Demonstration of an *in situ* on-chip tensile tester *J. Micromech. Microeng.* **19** 082001
- [14] Ouyang J and Zhu Y 2012 Z-shaped MEMS thermal actuators: piezoresistive self-sensing and preliminary results for feedback control *J. Microelectromech. Syst.* **21** 596–604
- [15] Mankame N D and Ananthasuresh G K 2001 Comprehensive thermal modelling and characterization of an electro-thermal-compliant microactuator *J. Micromech. Microeng.* **11** 452–62

- [16] Zhu Y, Corigliano A and Espinosa H D 2006 A thermal actuator for nanoscale *in situ* microscopy testing: design and characterization *J. Micromech. Microeng.* **16** 242–53
- [17] Pant B, Choi S, Baumert E K, Allen B L, Graham S, Gall K and Pierron O N 2012 MEMS-based nanomechanics: influence of MEMS design on test temperature *Exp. Mech.* **52** 607–17
- [18] Lott C D, McLain T W, Harb J N and Howell L L 2002 Modeling the thermal behavior of a surface-micromachined linear-displacement thermomechanical microactuator *Sensors Actuators A* **101** 239–50
- [19] Geisberger A A, Sarkar N, Ellis M and Skidmore G D 2003 Electrothermal properties and modeling of polysilicon microthermal actuators *J. Microelectromech. Syst.* **12** 513–23
- [20] Qin Q and Zhu Y 2013 Temperature control in thermal microactuators with applications to *in-situ* nanomechanical testing *Appl. Phys. Lett.* **102** 013101
- [21] Kearney S P, Phinney L M and Baker M S 2006 Spatially resolved temperature mapping of electrothermal actuators by surface Raman scattering *J. Microelectromech. Syst.* **15** 314–21
- [22] Liu C 2006 *Foundations of MEMS* (Englewood Cliffs, NJ: Prentice Hall)
- [23] Li L and Uttamchandani D 2009 Dynamic response modelling and characterization of a vertical electrothermal actuator *J. Micromech. Microeng.* **19** 075014
- [24] Sethu P and Mastrangelo C H 2003 Polyethylene glycol (PEG)-based actuator for nozzle-diffuser pumps in plastic microfluidic systems *Sensors Actuators A* **104** 7